Optical Materials 169 (2026) 117693

Contents lists available at ScienceDirect

Optical Materials

journal homepage: www.elsevier.com/locate/optmat

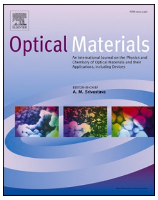

Research Article

Growth and multifaceted characterisation of phosphonium-based NLO single crystal: An efficient material for device and optical limiting applications

M. Mohanraj [a], T.C Sabari Girisun [b], M. Parthasarathy [a,*]

[a] Department of Physics, School of Basic Sciences, Vels Institute of Science, Technology and Advanced Studies, Pallavaram, Chennai, 600 117, Tamilnadu, India
[b] Nanophotonics Laboratory, School of Physics, Bharathidasan University, Tiruchirappalli, 620 024, Tamil Nadu, India

ARTICLE INFO

Keywords:
X-ray diffraction
Photoluminescence
Laser damage threshold
Photoconductivity
Electronic polarizability
Z-Scan analysis

ABSTRACT

Phosphonium-based nonlinear optical materials (NLO) are gaining attention due to their unique molecular structure, tunable electronic properties, and strong intermolecular interactions, making them promising candidates in photonics and optoelectronics. Recognising the vital importance of these materials, a potential NLO single crystal of Ethyltriphenylphosphonium iodide hydrate (ETPI) was grown using the low-temperature solution method, achieving dimensions of 45 × 10 × 3 mm^3 at ambient temperature for the first time. The XRD analysis indicates that the crystal belongs to the monoclinic system with a space group of $P2_{1/C}$. The vibrational assignments were confirmed through FT-IR analysis. Optical absorption analysis reveals a cutoff wavelength of 280 nm and an optical bandgap of 4.43 eV. Evaluating Urbach energy and optical constants indicates good optical quality with a low defect concentration. The photoluminescence (PL) spectrum distinctly shows that the material emits a striking violet light, characterised by its specific wavelength range. Surface morphology and elemental compositions were assessed by HR-SEM/EDAX analysis. The laser damage threshold (LDT) power density was 7.5 GW/cm^2, indicating its potential for high-power laser applications. The material exhibits negative photoconductivity, as evidenced by the observed photoconductive response. The thermal stability of the material was established through DSC analysis, revealing a melting point of 170 °C. The dielectric constant and loss exhibit an exponential decrease with increasing frequency and varying temperature. Theoretical assessments of electronic polarizability were conducted. Third-order NLO properties were determined using the Z-scan approach, including the absorption coefficient (β), saturation intensity (Is), and optical limiting threshold, which were found to be 0.84×10^{-10} m/W, 39×10^{11} W/m^2, and 3.41×10^{12} W/m^2, respectively. These outcomes highlight the crystal's suitability for integration into various nonlinear optical and photonic systems.

1. Introduction

The field of nonlinear optics is experiencing remarkable expansion, driven by its diverse applications, which span optical switching, optical modulation, and a wide array of photonic devices. To advance this field, developing new materials that exhibit exceptional optical transparency, robust resistance to laser exposure, and a pronounced non-linear response across an extensive frequency spectrum is of paramount importance [1]. Researchers are diligently working to synthesize effective materials tailored explicitly for nonlinear optical applications, with a keen focus on innovative classes of substances, including molecular-based compounds, organometallic compounds, and organic polymers. Organic materials stand out in this quest due to their cost-effectiveness, low dielectric constants, broad transparency ranges, notable thermal stability, and enhanced damage resistance [2]. The unique properties of organic compounds, particularly their conjugate donor-acceptor π systems, render them efficient derivatives for various applications in nonlinear optics [3]. Among the array of promising materials, phosphonium salts have garnered significant attention due to their distinctive characteristics and versatile applications across multiple scientific domains, including catalysis, organosynthesis, and electrochemistry [4]. Remarkably, phosphonium derivatives play a crucial role as nucleophiles in fluorination reactions, showcasing their versatility [5]. Furthermore, these compounds are employed in biocides,

---

[*] Corresponding author.
E-mail address: mps2k7@gmail.com (M. Parthasarathy).

https://doi.org/10.1016/j.optmat.2025.117693
Received 25 July 2025; Received in revised form 2 October 2025; Accepted 30 October 2025

plant growth regulators, and as photoinduced radical reagents, highlighting their practicality in real-world applications [6]. In the realm of triphenyl phosphonium compounds, the spatial arrangement of phenyl rings resembles a propeller-like structure, contributing to an extended and intricate overall geometry [7]. Triphenylphosphonium cations possess a remarkable capability to transport a diverse range of bioactive compounds, including antioxidants, dendrimers, and coenzymes, owing to their unique structural properties [8].

Ethyltriphenylphosphonium iodide hydrate is a quaternary phosphonium salt widely used in organic synthesis due to its distinctive reactivity and structural properties. This compound comprises a central phosphonium ion, which carries a positive charge, surrounded by three phenyl groups and an ethyl group. The presence of these bulky aromatic rings contributes to the overall stability and steric hindrance of the molecule, which can influence its reactivity in various chemical processes. The iodide ion serves as the counterion, playing a crucial role in maintaining the electrochemical balance of the compound. Additionally, the hydrate form indicates the presence of water molecules integrated into the crystal lattice, which can affect both the solubility and the reactivity of the salt in different solvents. Ethyltriphenylphosphonium iodide hydrate is particularly valued in synthetic organic chemistry for its applications in phase transfer catalysis, as well as in the synthesis of various organic compounds, making it an essential reagent in many laboratory settings.

A variety of phosphonium derivatives, such as Ethyltriphenylphosphonium bromide dihydrate [9], Methyltriphenyl phosphonium bromide hydrate [10], Methyltriphenylphosphonium iodide thiourea [11], Allyl triphenylphosphonium bromide [12], and Propyl triphenylphosphonium bromo chromate [13], demonstrate significant potential across multiple scientific fields, primarily due to their adaptable characteristics and innovative uses. While the crystal structure of Ethyltriphenylphosphonium iodide hydrate ($[(C_6H_5)_3P^+(I^-)C_2H_5]$. H_2O) has been elucidated [14], a comprehensive investigation into the physicochemical properties of this material remains lacking. Therefore, the primary objective of our current study is to grow high-quality, substantial single crystals of ETPI using the solvent evaporation method with a carefully selected mixed solvent of ethanol and distilled water. The resulting material will undergo a series of unprecedented characterisations, including PXRD, FT-IR, UV–Visible, Urbach energy assessment, the determination of optical constants, Photoluminescence studies, HR-SEM/EDAX, evaluation of laser damage threshold (LDT), analysis of photoconductivity, measurement of dielectric properties, assessment of polarizability, and potentially vital third-order nonlinear optical studies like Z-scan analyses were carried out. Remarkably, all these characterisations are reported here for the first time in the scientific literature.

2. Experimental procedure

The starting material used in this study was Ethyltriphenylphosphonium iodide, an analytically pure compound known for its exceptional quality and stability. A specific quantity of this reagent was accurately measured and then dissolved in a mixed solvent consisting of equal parts of ethanol and distilled water. To achieve a homogeneous solution, the resulting mixture was subjected to vigorous stirring for 6 h at a controlled temperature of 35 °C. This stirring process ensured the solution became completely soluble, which was then further filtered using Whatman filter paper. The filtered solution was then transferred into a thoroughly cleaned beaker, which was sealed with a polythene sheet punctuated with several small perforations. This setup was designed to permit controlled evaporation, allowing for slow, undisturbed evaporation in an environment free from mechanical vibrations and thermal fluctuations. After three weeks under these managed conditions, the evaporation process successfully yielded a clear, good-quality single crystal of Ethyltriphenylphosphonium iodide hydrate (ETPI). The dimensions of the crystal measured an impressive 45 mm × 10 mm × 3 mm, as shown in Fig. 1.

3. Results and discussion

3.1. X-ray diffraction analysis

The as-grown single crystal of ETPI was subjected to X-ray diffraction analysis using an ENRAF NONIUS CAD4 diffractometer. The data obtained indicate that the material is classified as monoclinic, with a space group of $P2_{1/C}$. The lattice parameters are as follows: $a = 10.831(15)$ Å, $b = 14.502(2)$ Å, and $c = 12.951(19)$ Å, with angles $\alpha = \gamma = 90^\circ$ and $\beta = 102.39(3)^\circ$. These measurements align well with those previously reported [14] as presented in Table 1. Furthermore, the Powder X-ray diffraction (PXRD) analysis, conducted using a PANalytical diffractometer with CuKα radiation ($\lambda = 1.5418$ Å) over an angular range of 10°–70°, shows sharp and well-defined diffraction peaks, as shown in Fig. 2. The absence of unindexed reflections or additional peaks indicates that no secondary phases or domains are present in the grown material. The prominent peaks from the experimental measurements have been compared to those from theoretical calculations, reinforcing the consistency of the PXRD data with the single-crystal XRD results.

3.2. FT-IR spectral analysis

The Fourier Transform Infrared (FT-IR) spectrum of the ETPI sample was carefully recorded over the range of 400–4000 cm^{-1} using a Bruker 66V FT-IR spectrometer from a finely powdered form of the crystal used in this study. A small piece of the crystal was carefully ground to a uniform consistency and mixed with high-purity spectroscopic-grade potassium bromide (KBr). This mixture was then pressed into a transparent pellet, ensuring precise and consistent spectral analysis. As depicted in Fig. 3, the FT-IR spectrum of the compound under investigation reveals a tapestry of notable peaks, each carrying significant information. These peaks correspond to the distinct vibrational movements of chemical bonds within the sample, offering invaluable insights into its molecular architecture and the presence of various functional groups [15]**.** A closer inspection of these peaks promises to deepen our understanding of the compound's properties. Notably, the broad peak observed at 3409 cm^{-1} is particularly striking, which can be attributed to the O–H stretching vibration of water, indicating the compound's potential for hydration. The peaks at 2924 cm^{-1} and 2883 cm^{-1} correspond to the CH_2 vibrations associated with the ethyl group, highlighting the presence of this aliphatic component in the molecule. Moreover, the bending mode of water is evident at 1636 cm^{-1}, emphasising the compound's interaction with moisture. The peaks at 1486 cm^{-1} and 1437 cm^{-1} resonate with the vibrations of the aromatic ring embedded within the compound, revealing the structural complexity that aromatic compounds are known for. The significant peaks at 1384 cm^{-1} and 1341 cm^{-1} can be attributed to the bending vibrations of the CH_2 group, further elucidating the compound's aliphatic character.

Additionally, the peaks at 1264 cm^{-1}, 1164 cm^{-1}, 1033 cm^{-1}, and 996 cm^{-1} indicate P–C vibrations, offering insight into potential phosphorus interactions within the molecular framework. Finally, the peaks at 861 cm^{-1}, 755 cm^{-1}, and 689 cm^{-1} correspond to the bending vibrations of aromatic C–H bonds, indicating a rich and intricate network of vibrations characteristic of aromatic compounds. This complex pattern of observed peaks underscores the multifaceted interactions within the molecular structure, highlighting the compound's rich chemical landscape [16]**.**

3.3. Optical studies

3.3.1. UV–visible absorbance analysis

UV–Visible analysis serves as a crucial analytical technique for uncovering intricate details about a material's optical transparency and the electronic transitions occurring within its molecular structure. The absorption studies were meticulously performed across a wavelength

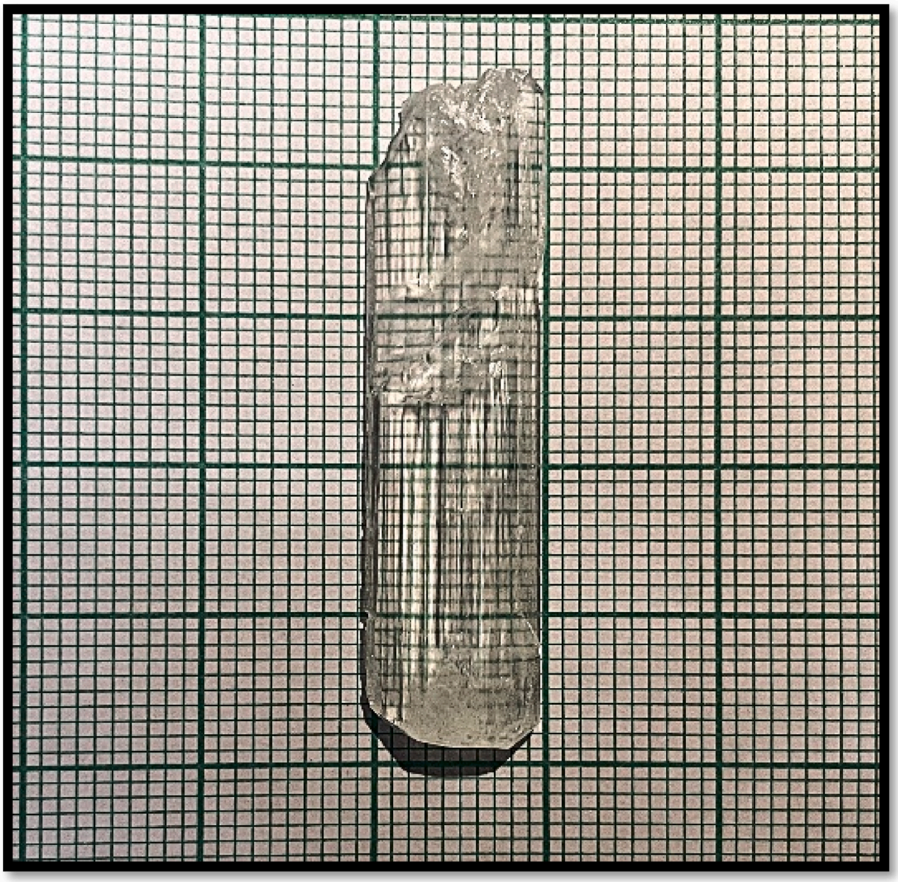

Fig. 1. As-grown single crystal of ETPI.

Table 1
Single-crystal XRD parameters of ETPI.

Lattice Parameters	Present Work	Pavel Valerievich Andreev et al. [14]
a (Å)	10.831(15)	10.805(2)
b (Å)	14.502(2)	14.276(3)
c (Å)	12.951(19)	12.974(3)
$\alpha = \gamma$ (°)	90	90
β (°)	102.39(3)	102.67(2)
Crystal System	Monoclinic	Monoclinic
Space group	$P2_{1/C}$	$P2_{1/C}$

spectrum ranging from 200 nm to 800 nm. As depicted in Fig. 4(a), the material exhibits a striking cut-off wavelength at 280 nm, a significant point that reflects its distinctive optical behaviour. The presence of the triphenylphosphonium moiety, characterised by its aromatic rings, contributes to absorption in the ultraviolet range, primarily due to $\pi \rightarrow \pi^*$ transitions. This pronounced cut-off at 280 nm can be attributed to these aromatic systems, which play a pivotal role in the material's optical properties. Such attributes position the material as an exceptionally promising candidate for innovative nonlinear optical and optoelectronic applications. The material's remarkably low absorption throughout the entire UV–visible spectrum, combined with an extensive transparency window, further enhances its appeal for potential applications in advanced optical technologies [17].

To quantitatively evaluate the absorption characteristics, Tauc's relationship (1) can be employed to determine the absorption coefficient:

$$(\alpha h\nu)^n = T\,(h\nu - Eg) \tag{1}$$

In this particular equation, the exponent value of $n = 1/2$ signifies a direct bandgap, while an exponent of $n = 2$ indicates an indirect bandgap. Tauc's plot, illustrated in Fig. 4(b), offers a visual representation that shows the optical bandgap energy of the material is approximately 4.43 eV. This figure is not merely a theoretical construct; it is validated by Planck's equation, represented as [$E = hc/\lambda$]. Within this context, λc denotes the cut-off wavelength associated with the material, and the ensuing calculations corroborate the bandgap energy at 4.43 eV. This result aligns seamlessly with experimental observations, reinforcing the accuracy of the measurements. The implications of these findings are significant, suggesting that the material possesses enhanced optical conductivity. This remarkable property enables the material to absorb photon energy efficiently, thereby expanding its potential applications across various fields, including advanced photonic fabrication and innovative third-harmonic generation processes [18]. Such capabilities underscore the material's promise in cutting-edge technological developments and applications.

3.3.2. *Absorption band tail*

The presence of disorders often leads to band tailing in crystalline materials due to the interaction of phonons in the bandgap region. The Urbach energy, characterised by an exponential tail, significantly influences materials with minimal crystallinity, while its impact is considerably diminished for well-crystalline materials [19]. An exponential equation, known as the Urbach empirical rule (2–3), delineates the correlation between the absorption coefficient (α) and photon energy [20].

$$\alpha = \alpha_o \exp\left(\frac{h\nu}{E_u}\right) \tag{2}$$

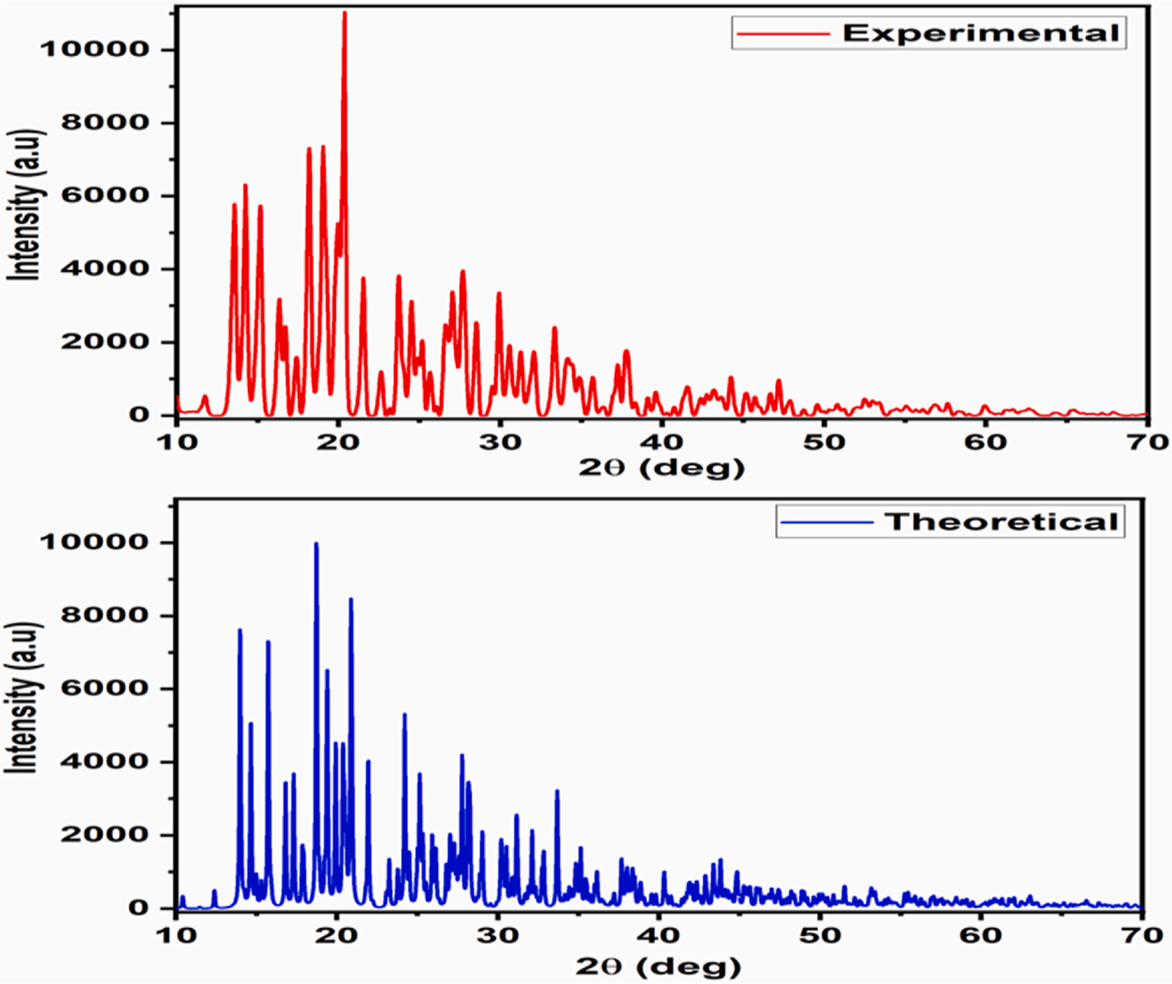

Fig. 2. Experimental and Theoretical XRD pattern of ETPI.

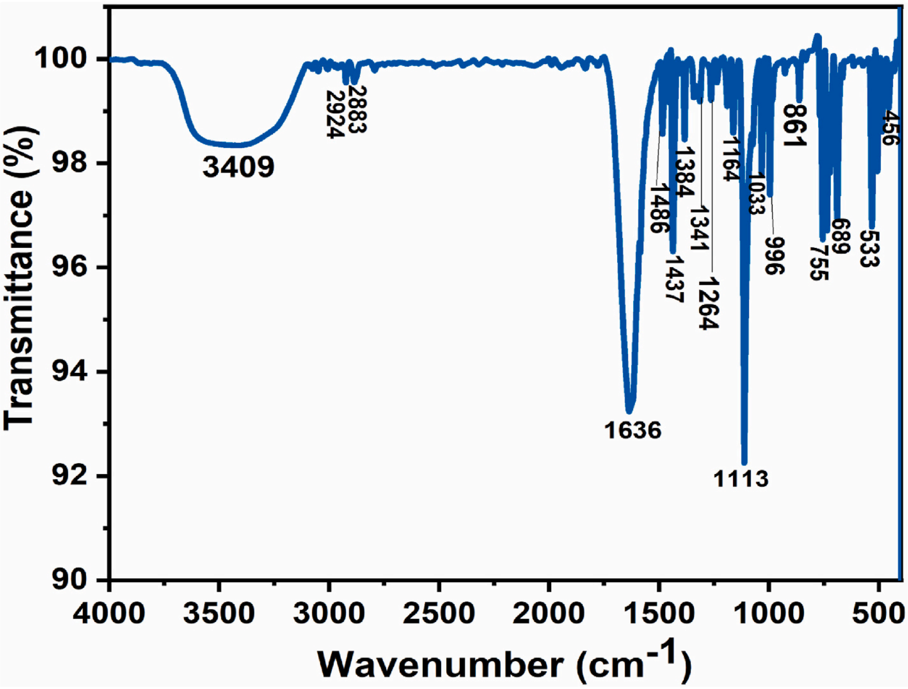

Fig. 3. FT-IR spectrum of ETPI.

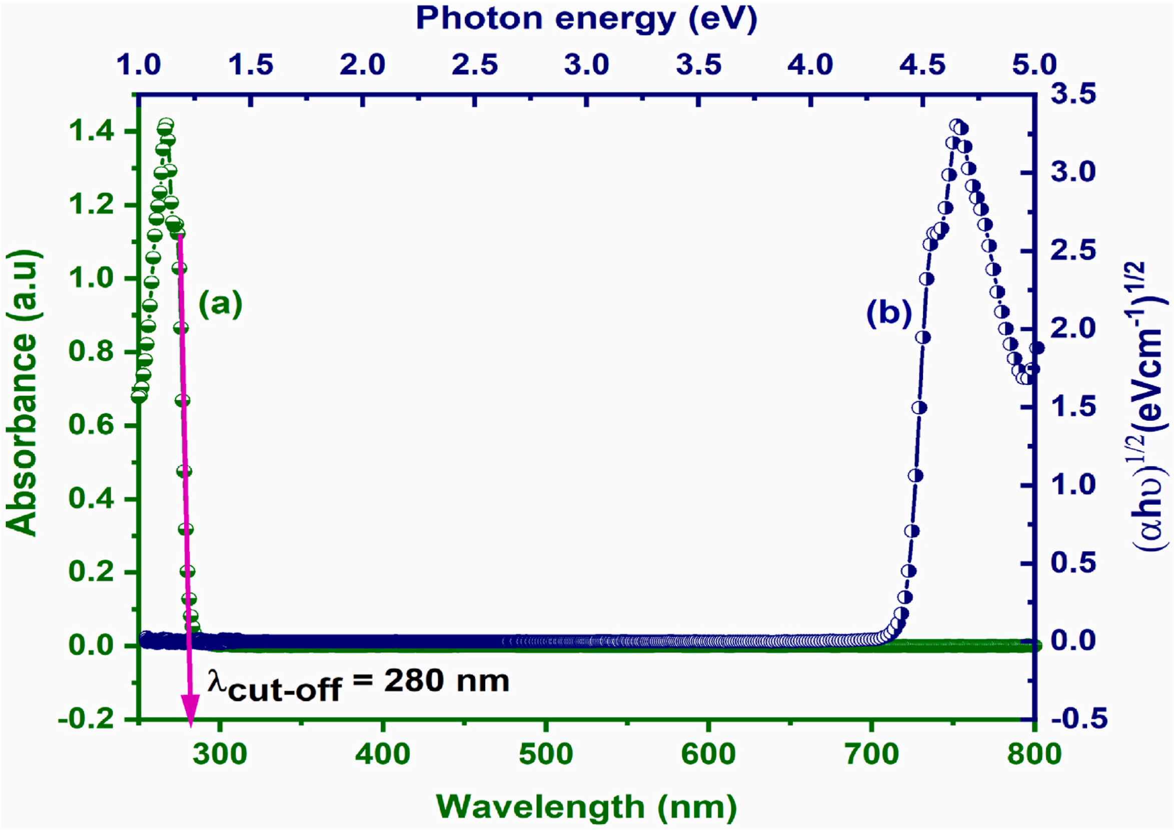

Fig. 4. **(a)** UV–Visible absorbance spectrum **(b)** Plot of $(\alpha h\nu)^{1/2}$ vs Photon energy ($h\nu$).

$$\ln(\alpha) = \ln\,(\alpha_o) + \frac{h\nu}{E_u} \tag{3}$$

This equation presents a representation of the Urbach energy as provided by the E_U. Fig. 5 illustrates the relationship between photon energy and ln(α), with a slope of 8.009. Taking the reciprocal yields the Urbach energy E_U, measured at 0.125 eV. This result indicates that the material exhibits high crystallinity and a low concentration of flaws. Furthermore, Urbach formulated an additional correlation between the absorption coefficient and the optical bandgap [21], as specified in Equations (4) and (5).

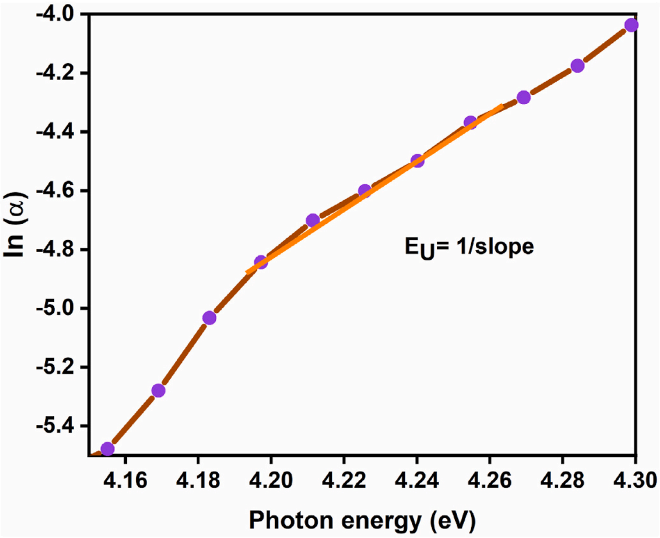

Fig. 5. Plot of ln (α) vs Photon energy ($h\nu$).

$$\alpha = \beta \exp\left[\frac{\sigma(h\nu - E_o)}{K_B T}\right] \tag{4}$$

where β is a pre-exponential constant and σ is another constant called the steepness parameter. E_O is the transition energy, which equals Eg for a direct allowed transition. However, for an indirect transition, it equals Eg ± Ep, where Ep is the energy of the phonon, which mainly influences the bandgap energy because of thermal dissociation of the lattice sites. The ETPI crystal has a direct bandgap and hence $E_0 = E_g$, and taking the logarithm on both sides of equation (4) and comparing with equation (3), it can be rewritten as follows:

$$\left(\frac{h\nu}{E_U}\right) = \left(\frac{\sigma(h\nu)}{K_B T}\right) \tag{5}$$

In this context, E_U equals 0.125 eV; K_B signifies the Boltzmann constant; and T symbolises the absolute temperature. The steepness parameter (σ) is found by equation (6),

$$\sigma = \frac{K_B T}{E_U} \tag{6}$$

resulting in a value of 0.189. Additionally, the strength of the electron-photon interaction ($E_{e\text{-}p}$) is calculated using equation (7),

$$E_{e-p} = \frac{2}{3\sigma} \tag{7}$$

resulting in a magnitude of 3.537. Table 2 summarises the details for the cut-off wavelength (nm), optical band gap energy (E_g), Urbach energy (E_U), steepness parameter (σ), and electron-photon energy ($E_{e\text{-}p}$), indicating that the material has excellent crystal quality, good response to phonons, and strong potential for making photonic devices [22].

Table 2
Urbach energy and its parameters.

Description	Value
Wavelength of absorption edge (nm)	280 nm
Optical bandgap (E_g)	4.43 eV
Urbach energy (E_U)	0.125 eV
Steepness parameter (σ)	0.189
Electron-photon interaction energy ($E_{e\text{-}p}$)	3.537

3.3.3. *Determination of optical constants*

This entails a meticulous examination of optical constants, including optical conductivity, refractive index, and extinction coefficient, which are crucial in determining the optical behaviour of materials and their applicability in optoelectronics, optical switching, and various nonlinear optical applications [23]. The material's composition and reflective characteristics exclusively determine the refractive index. Equation (8) computes the refractive index of the material based on the reflectance data [24].

$$n=\frac{-(R+1)\pm\sqrt{(-3R^2+10R-3)}}{2(R-1)} \tag{8}$$

The resultant graph, Fig. 6(a), demonstrates that the refractive index of the material is 1.3708 at a wavelength of 532 nm. The refractive index denotes the degree to which light is refracted or bent upon entering the substance. The reduced refractive index and high transmission across the whole visible spectrum led to significant advancements in the field of optoelectronics [25].

The extinction coefficient measures a substance's capacity to absorb or reflect light at a specific wavelength and signifies the degree of absorption loss when electromagnetic waves traverse the material [26]. The computation can be executed via equation (9).

$$K=\frac{\alpha\lambda}{4\pi} \tag{9}$$

Fig. 6(b) illustrates that the extinction coefficient of the material increases with higher photon energy, indicating an enhanced response to light intensity. The minimum attenuation coefficient at diminished photon energy makes the material suitable for device development [27].

3.4. *Photoluminescence studies*

The Fluorolog-3-11 spectrometer was utilised for an extensive photoluminescence analysis of the title compound. A 450 W xenon lamp powers it, offers a resolution of 0.2 nm and covers a wavelength range from 180 to 850 nm. Photoluminescence (PL) involves the spontaneous emission of light following photoexcitation, influenced by mechanisms such as internal conversion, intersystem crossing, and vibrational relaxation [28]. During the examination, the compound was excited at around 270 nm, resulting in a notable emission peak at 300 nm. The spectra, illustrated in Fig. 7, indicate a striking violet light emission, reflecting the material's high quality and minimal defects. Additionally, the temporal analysis of the emission reveals diverse energy levels and their lifetimes, underscoring the material's potential for organic scintillator applications and device fabrication [29].

3.5. *HR-SEM/EDAX analysis*

The surface morphology of the material was meticulously analysed using a Quanta 200FEG high-resolution scanning electron microscope (HR-SEM), which is renowned for its exceptional imaging capabilities. Fig. 8 presents the HR-SEM images captured at various magnifications, employing an acceleration voltage of 30 kV to ensure optimal resolution and clarity. The images reveal that the material possesses a distinct agglomerated morphology, characterised by clustered particles, which facilitates the observation of microcrystalline structures intricately woven into its growth pattern [30].

To further investigate the material's composition, Energy-Dispersive X-ray Spectroscopy (EDAX) analysis was conducted, providing a comprehensive assessment of the elemental constituents present. The EDAX spectrum, illustrated in Fig. 9, reveals significant peaks corresponding to various elements. The EDAX spectrum confirms the elemental composition of the grown ETPI crystal, indicating the

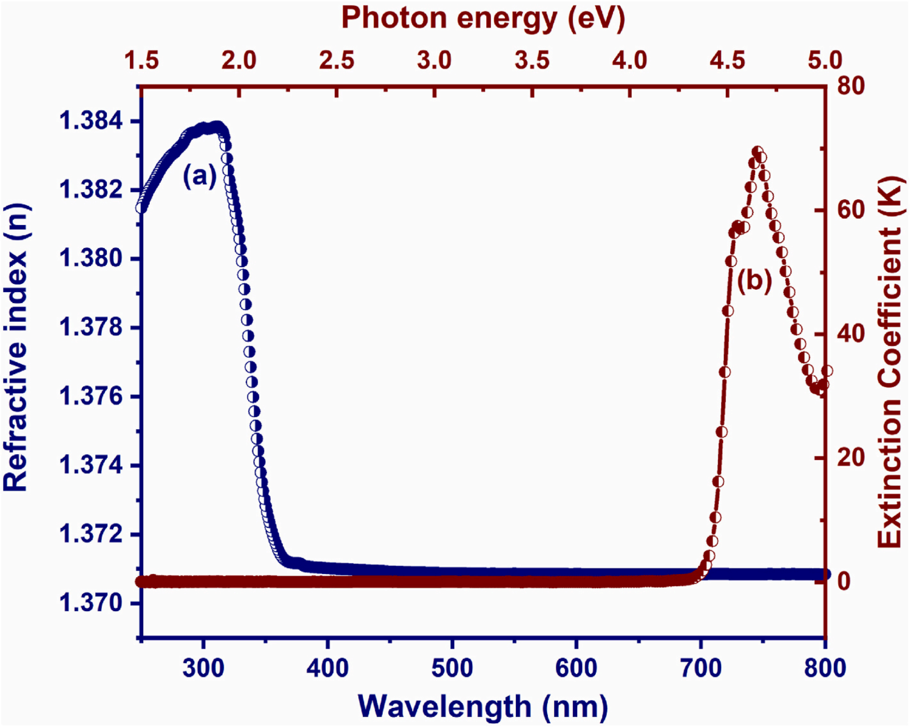

Fig. 6. Plot of **(a)** Refractive index (n) vs Wavelength (nm) **(b)** Extinction coefficient (K) vs Photon energy (hν).

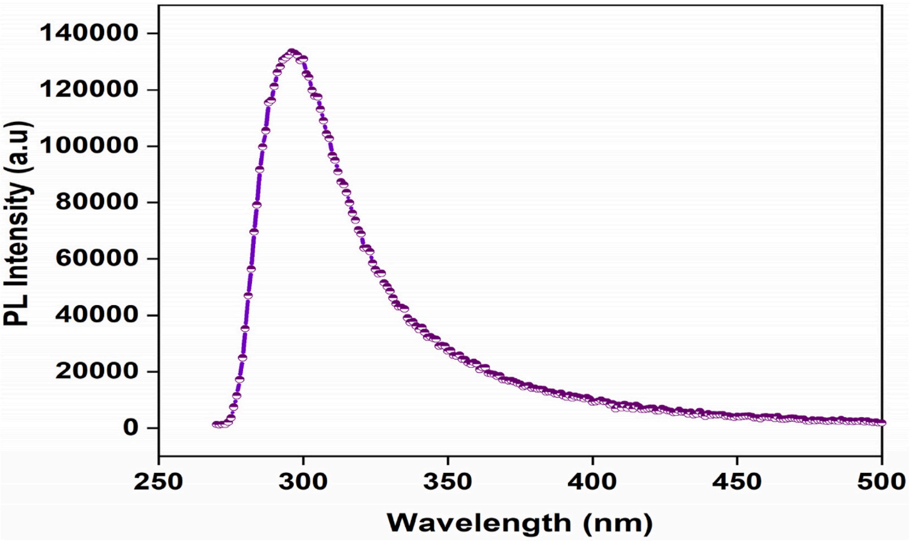

Fig. 7. PL spectrum of ETPI.

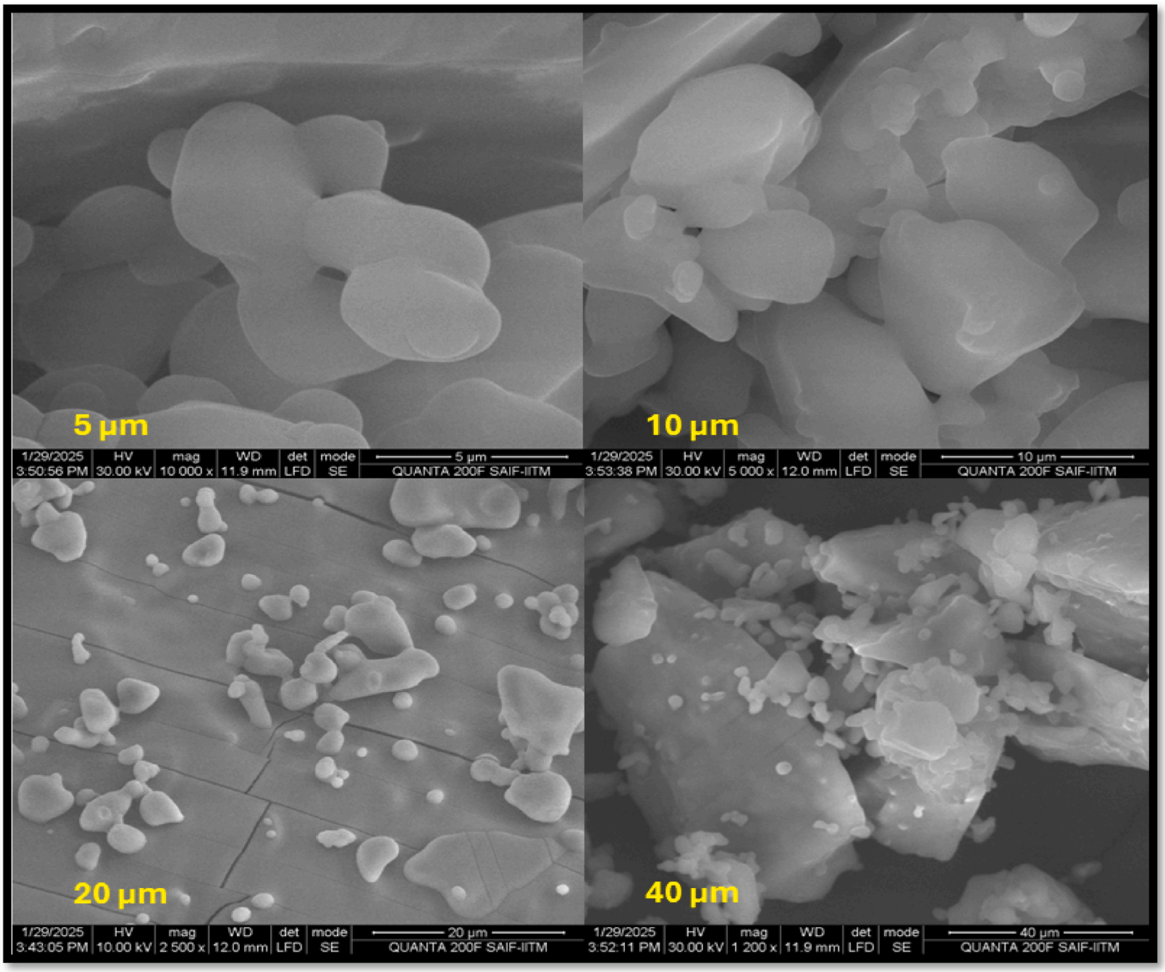

Fig. 8. HR-SEM images of ETPI.

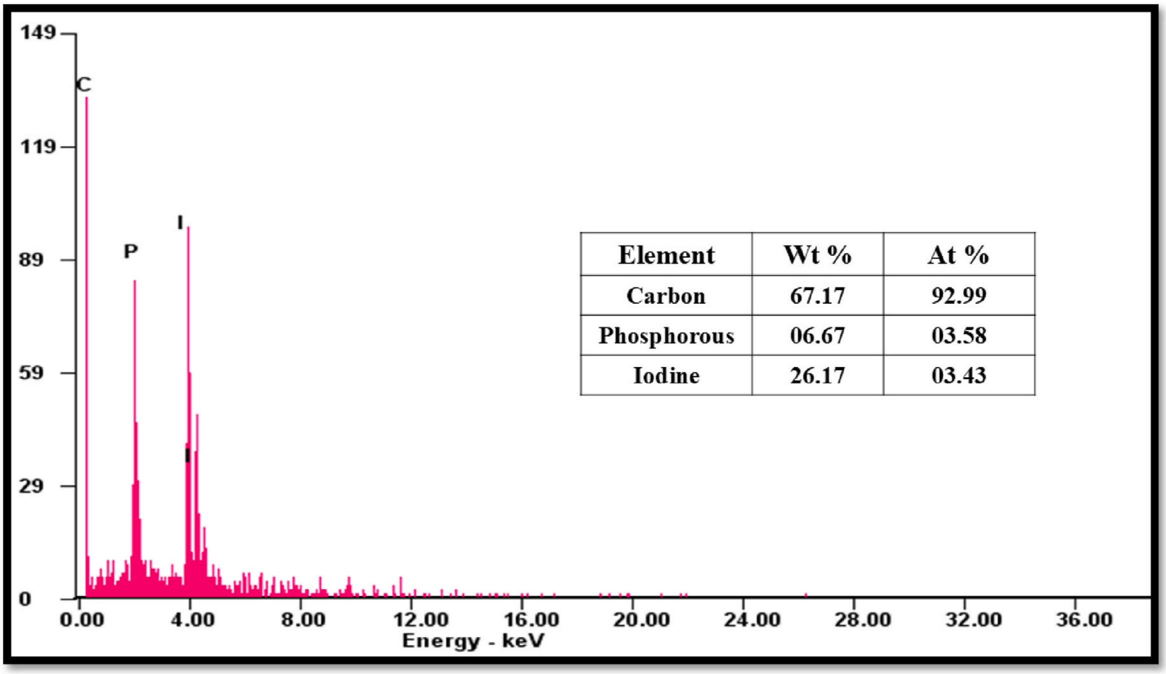

Element	Wt %	At %
Carbon	67.17	92.99
Phosphorous	06.67	03.58
Iodine	26.17	03.43

Fig. 9. EDAX spectrum of ETPI

presence of only Carbon, Phosphorus, and Iodine in the expected stoichiometric ratios (Carbon = 67.17 wt%, Phosphorus = 6.67 wt%, Iodine = 26.17 wt%), without any detectable extraneous elements. This evidence supports the chemical purity of the material and further confirms the absence of any additional structural phases.

3.6. *Laser damage threshold studies*

The laser damage threshold of the material is influenced by a variety of intricate physical processes, including electron avalanche, photoionisation driven by heat absorption, photochemical breakdown, multiphoton absorption, and electrostrictive fracture [31]. The efficacy of a nonlinear optical (NLO) material hinges not only on its inherent optical, thermal, and mechanical characteristics but also on the robustness of its surface in enduring high-power levels. To evaluate the material's resistance to laser-induced damage, a precise experimental setup was established using a single-shot Nd-YAG laser source operating at a frequency of 10 Hz with adjustable energy output. In this setup, a beam splitter intricately divided the incoming laser beam into two equal-energy segments. One segment served as a reference point, while the other was directed toward the polished surface of the crystal through a converging lens with a focal length of 10 cm. As illustrated in Fig. 10 (a), the crystal's surface was examined before exposure to the laser beam. Following irradiation, the crystal underwent significant thermal stress and melting, consequences of the intense energy delivered by the laser pulse, which resulted in visibly apparent damage and a distinct, startling cracking sound. The damages inflicted by the high laser intensity are depicted in detail in Fig. 10(b), showcasing the catastrophic

Table 3
Comparison of the LDT values with other NLO single crystals.

NLO materials	Power Density (GW/ cm^2)
L-Histidinium phthalate iodide [32]	1.29 GW/cm^2
l-Proline Potassium Iodide [33]	2.14 GW/cm^2
l-Serine Phosphate [34]	5.27 GW/cm^2
Ethyltriphenylphosphonium Iodide hydrate [present work]	7.50 GW/cm^2

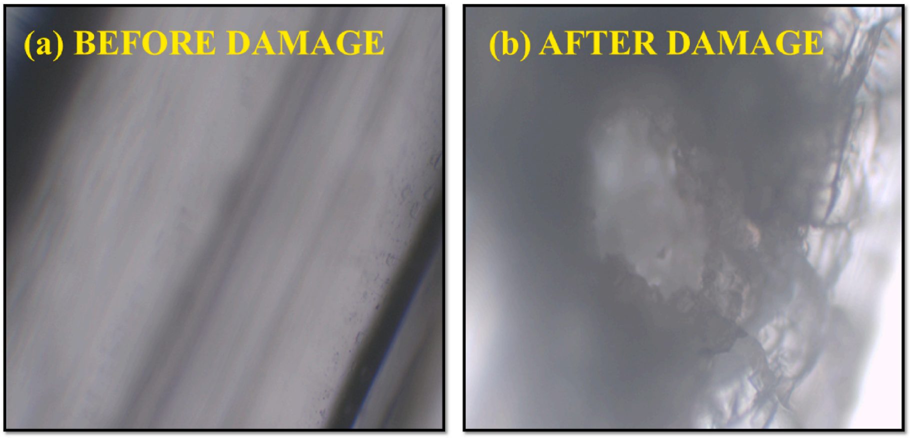

Fig. 10. Laser Damage view pattern (a) before (b) after.

effects of thermal stress on the crystal's integrity.

The power density was calculated using equation (10),

$$\mathrm{P_d} = \frac{E_p}{\tau\pi\omega_0{}^2} \tag{10}$$

The resulting calculated power density of the crystal reached an impressive 7.5 GW/cm^2. As shown in Table 3, this power density notably surpasses that of many currently known nonlinear optical materials [32–34]. Such a remarkable power density indicates that these materials hold substantial promise as potential candidates for advanced applications in high-power laser systems and in the expanding field of nonlinear optics.

3.7. Photoconductivity studies

The photoconductivity of the material is influenced by several key factors, including temperature, light intensity, the applied electric field, carrier density, and the lifespan of the charge carriers [35]. In this study, the photoconductivity of the specified material was meticulously evaluated using a Keithley Picoammeter (Model M6487). The sample was carefully positioned in contact with a bimetallic electrode, employing silver paste to ensure optimal electrical connectivity. Following this, the sample was securely fastened to the cold finger within the cryostat, where precise temperature control is paramount for accurate measurements. The experimental setup featured two electrodes connected to a DC power supply, which enabled the application of a variable potential ranging from 1 to 50 V, adjusted in 1 V increments throughout the test. To assess the device's performance in different conditions, the dark current (I_D) was measured at various voltages, ensuring that the sample remained unilluminated during this phase to eliminate any influence from light. Subsequently, the photocurrent (I_P) was recorded under diverse light irradiation and voltage settings, allowing for a comprehensive analysis of the material's behaviour. As illustrated in Fig. 11, there is a clear correlation between the photocurrent and dark current in relation to the applied voltage. The data reveal a significant increase in both photocurrent and dark current with rising voltage levels [36]. Interestingly, the dark current consistently surpassed the photocurrent, indicating the material's unique negative photoconductive characteristics.

This negative photoconductivity phenomenon occurs due to a decrease in the number of charge carriers or a reduction in their lifetime when subjected to radiation. Such a decrease in carrier lifespan enhances the trapping process and increases the velocity of the carriers, reinforcing the material's distinctive behaviour [37]. Numerous studies have documented materials that exhibit similar negative photoconductive properties, including notable examples such as L-Alanine hydrogen chloride [38], Bisglycine hydrobromide [39], L-Phenylalanine-4-nitrophenol [40], and L-Asparagine [41], each contributing to an expanding understanding of this intriguing phenomenon.

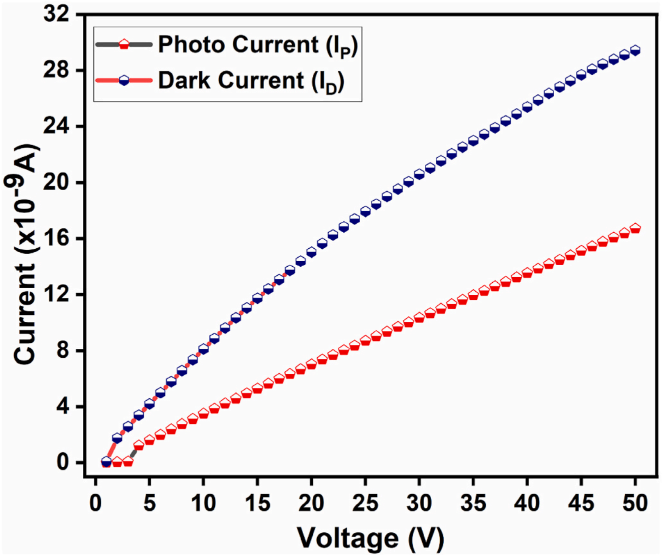

Fig. 11. Field-dependent photoconductivity of ETPI.

3.8. Thermal analysis

The Differential Scanning Calorimetry (DSC) analysis of the specified substance was meticulously conducted over an extensive temperature range of 25 °C–500 °C at a controlled heating rate of 10 K/min, using a state-of-the-art NETZSCH STA 409C analyser in a nitrogen atmosphere. This advanced DSC technique was instrumental in unravelling the thermal properties of the material, focusing on crucial metrics such as the melting point and the intricate thermal energy transitions [42].

The initial exothermic peak, clearly illustrated in Fig. 12, reveals that the melting point of ETPI occurs at 170 °C, marking a significant transition in its thermal behaviour. Following this, the second exothermic peak observed at 365 °C signifies the decomposition of organic residues, highlighting the material's thermal degradation process. This distinctive thermal profile not only showcases the material's impressive thermal stability but also underscores its capability to withstand high-temperature laser applications effectively [43].

3.9. Dielectric studies

The dielectric characteristics of the material are profoundly intertwined with its lattice dynamics, providing essential insights into the fundamental atomic qualities, defect concentration, bonding interactions, and polarisation mechanisms inherent within the structure. This meticulously fabricated crystal, boasting exceptional optical clarity and purity, was specifically used for comprehensive dielectric investigations [44]. To facilitate these studies, a thin layer of silver was applied to the opposing surfaces of the crystal and strategically positioned between two copper electrodes, effectively creating a parallel plate capacitor. The capacitance of the material was meticulously measured across an extensive range of frequencies and temperatures, extending from ambient conditions to a remarkable 140 °C. The dielectric constant, a pivotal parameter, is articulated through equation (11):

$$\varepsilon' = \frac{C_p d}{\varepsilon_0 A} \tag{11}$$

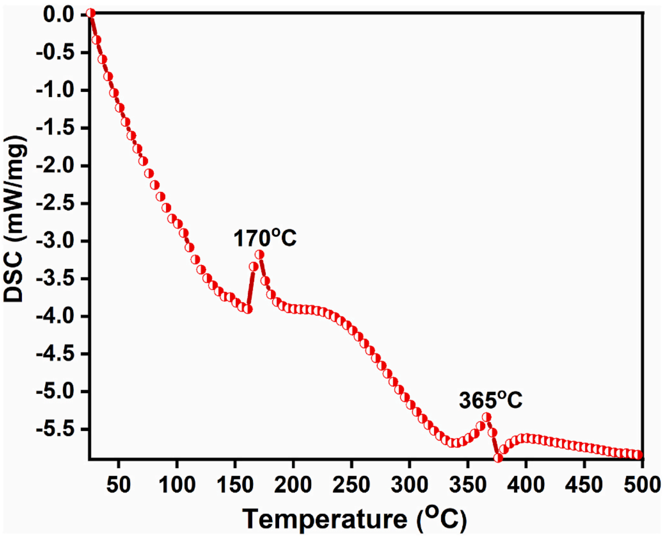

Fig. 12. DSC trace of ETPI.

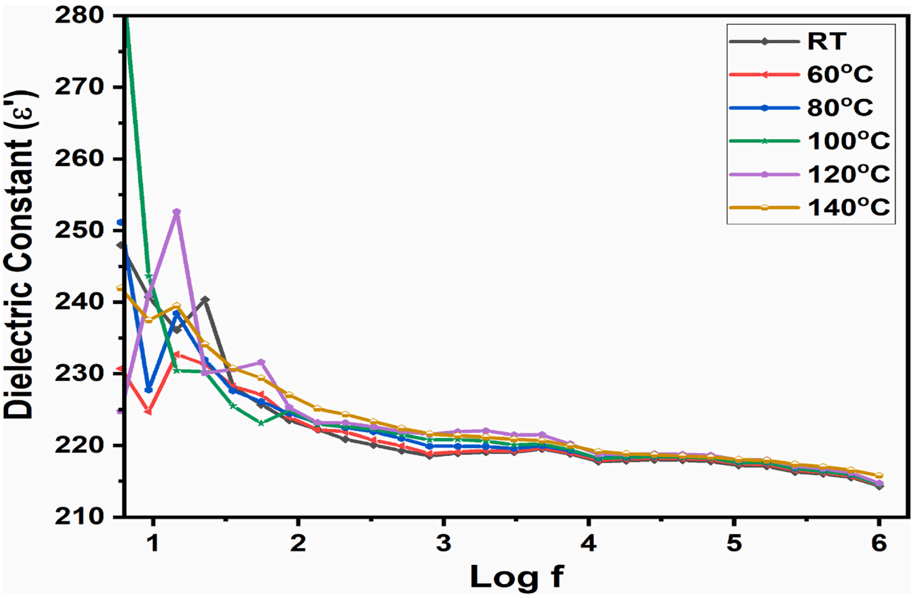

Fig. 13. Dielectric constant (ε') vs Log f.

As illustrated in Fig. 13, the dielectric constant exhibits a pronounced increase at low frequencies, gradually tapering off as the frequency rises, ultimately reaching a stable equilibrium at higher frequencies across varying temperatures. This signifies the static dielectric constant. The elevated dielectric constant observed at lower frequencies can be attributed to a plethora of polarisation phenomena, including interfacial, dipolar, ionic, and electronic polarisation. However, as frequency escalates, a notable reduction in polarisation occurs, leading to a misalignment between the applied electric field and the dipole moment, ultimately resulting in diminished polarisation efficacy beyond a critical frequency [45]. Fig. 14 further elucidates this behaviour, demonstrating that the material experiences minimal dielectric loss at elevated frequencies, eventually stabilising, which signals a lack of defects or imperfections within the crystal structure and underscores its superior optical quality. Materials characterized by low dielectric constants and minimal dielectric loss are particularly promising candidates for a wide range of applications in laser technology, photonics, microelectronics, and electro-optic systems [46].

3.10. Polarizability studies

The electrical polarizability of a material is fundamentally linked to its response when subjected to an external electric field. This characteristic plays a crucial role in determining how frequency conversion occurs within that material, as its polarizability entirely governs it. Numerous theoretical approaches have been developed to ascertain the electronic polarizability of various substances. Among these methods, notable examples include the Penn gap, Clausius–Mossotti relation, the optical bandgap, and the coupled dipole method [47,48]. To explore the calculations related to the Penn gap, valence electron plasma energy, Fermi energy, and, of course, electronic polarizability, one would start by determining the density (ρ) of the substance in question, an essential

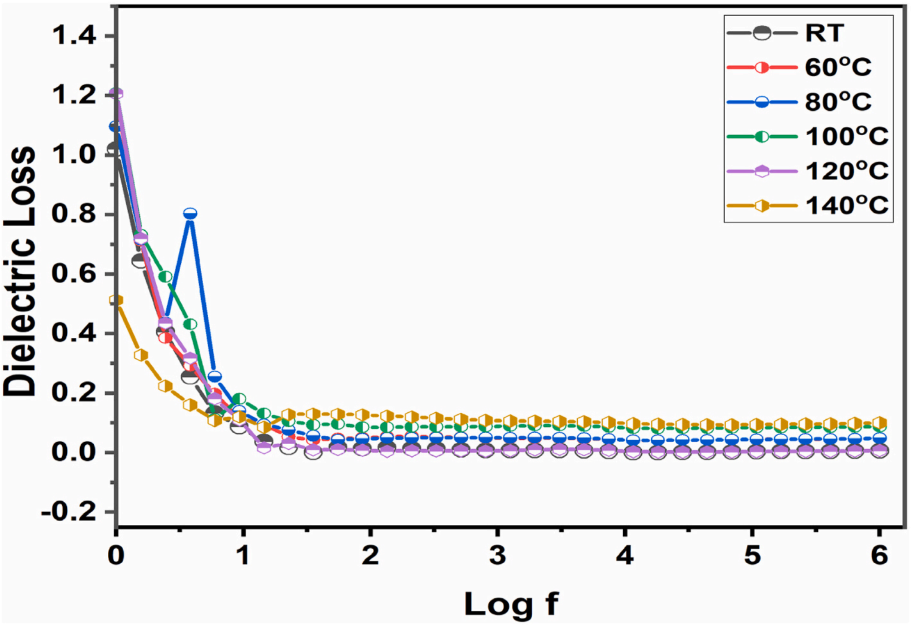

Fig. 14. Dielectric loss vs Log f.

step that can be computed using equation (12). This foundational parameter lays the groundwork for a deeper understanding of the material's electronic properties and behavior under electrical influences.

$$\rho = \frac{MZ}{N_A V} \, \mathrm{g} \Big/ \mathrm{cm}^3 \tag{12}$$

The valence electron plasma energy (ħ ω_p) [49] is determined using equation (13)

$$\hbar\omega_p = 28.8\left(\frac{z' x \rho}{M}\right)^{1/2} \tag{13}$$

The Fermi energy (E_F) and Penn gap (E_P) [50] can be determined from the valence electron plasma energy using the following equations 14 and 15:

$$E_F = 0.2947\left(\hbar\omega_p\right)^{4/3}\mathrm{eV} \tag{14}$$

$$E_P = \frac{\hbar\omega_p}{(\varepsilon - 1)^{1/2}} \ \mathrm{eV} \tag{15}$$

As a result, electronic polarizability (α) [51] is determined using the following equation (16)

$$\alpha = \left[\frac{\left(\hbar\omega_p\right)^2 S_0}{\left(\hbar\omega_p\right)^2 S_0 + 3{E_P}^2}\right] \times \frac{M}{\rho} \times 0.396 \times 10^{-24} cm^3 \tag{16}$$

S_0 represents a constant that is specific to the material [52], as defined by equation (17)

$$S_0 = 1 - \left[\frac{E_P}{4E_F}\right] + \frac{1}{3}\left[\frac{E_P}{4E_F}\right]^2 \tag{17}$$

The Clausius–Mossotti relation expresses the electronic polarizability (α), which is directly linked to the dielectric constant of the material [53], as follows (18)

$$\alpha = \frac{3M}{\pi N_A \rho}\left[\frac{\varepsilon' - 1}{\varepsilon' + 2}\right] cm^3 \tag{18}$$

The electrical polarizability (α) is related to the optical bandgap by the following equation: (19)

$$\alpha = \left[1 - \frac{\sqrt{E_g}}{4.06}\right] \times \frac{M}{\rho} \times 0.396 \times 10^{-24} cm^3 \tag{19}$$

The dipole moment frequently emerges in response to an external electric field. The electronic polarizability (α) is determined through the coupled dipole method [54,55] using the specified equation. (20)

$$\alpha = \frac{Z' e^2}{m_e \omega_0^2} \tag{20}$$

The resulting crystal demonstrates significant polarisation capability, indicating improved sensitivity to electric fields and exceptional optical quality [56]. The calculated electronic polarizability and solid-state parameters of the material are presented in Table 4, which suggests a reduced concentration of defects.

Table 4
Polarizability value of ETPI.

Electronic polarizability (α)	Ethyltriphenylphosphonium iodide hydrate (Present work)
Plasma energy	17.428 (eV)
Fermi energy	45.185 (eV)
Penn gap	1.1941 (eV)
Penn analysis (α)	11.30×10^{-23} cm^3
Clausius– Mossotti relation (α)	11.37×10^{-23} cm^3
Optical band gap (α)	5.79×10^{-23} cm^3
Coupled dipole method (α)	7.56×10^{-23} cm^3

3.11. Third order nonlinear optical studies (Z-scan)

The nonlinear absorption and optical limiting properties of ETPI were studied using the single-beam Z-Scan technique [57]. This approach examines the material's optical properties by analysing light interactions, focusing on transmittance affected by nonlinear absorption. A Q-switched Nd: YAG laser (Quanta-Ray INDI-10) with a 9 ns pulse width and 532 nm wavelength was employed. To prepare the sample, 0.15 mg of powdered ETPI was dispersed in 5 mL of ethylene glycol, resulting in a linear transmittance of 70 %. Ethylene glycol primarily serves as a polar solvent, enhancing the activity of solutes while exhibiting no notable nonlinear optical response. A Z-scan conducted under the specified experimental conditions on pure ethylene glycol reveals an absence of nonlinear characteristics. Consequently, it does not affect the nonlinear absorption of the ETPI sample. Key experimental parameters included a Rayleigh range of 1.69 mm, a beam waist of 16.9 μm and a pulse energy of 100 μJ. A convex lens with a 15 cm focal length focused the laser beam on the sample in a 1 mm quartz cuvette. The beam was scanned over 100 mm in set steps, showing how the absorption coefficient varies with increasing light intensity.

The prominent nonlinear absorption (NLA) characteristics of the sample display both saturable absorption (SA) and reverse saturable absorption (RSA) behaviours. In the case of saturable absorption, the nonlinear transmission reaches its maximum at the focal point of the laser beam, exhibiting a distinct peak in the open-aperture Z-scan traces. Conversely, reverse saturable absorption exhibits a clear valley-like profile, indicating maximum absorption at the focus. The nonlinear absorption coefficient (β) is a key parameter; a positive β indicates RSA, while a negative β signifies SA. Thus, the peak associated with saturable absorption or the valley related to reverse saturable absorption, similar to an open-aperture Z-scan pattern, reveals the type of nonlinear optical absorption of the material. In this study, the open-aperture Z-scan curves show a distinctly valley-shaped profile, confirming that the primary NLA mechanism is reverse saturable absorption. Fig. 15 shows the open-aperture curve of ETPI, with the normalised transmission calculated using Equation (21):

$$T(z) = \frac{1}{\sqrt{\pi q(z)}} \int_{-\infty}^{+\infty} \ln\left[1 + q(z)\exp\left(-\tau^2\right)\right] d\tau \tag{21}$$

where $q(z) = \beta L_{eff} \frac{I_\circ}{\left(1 + \left(\frac{Z}{Z_\circ}\right)^2\right)}$, β is the nonlinear absorption coefficient,

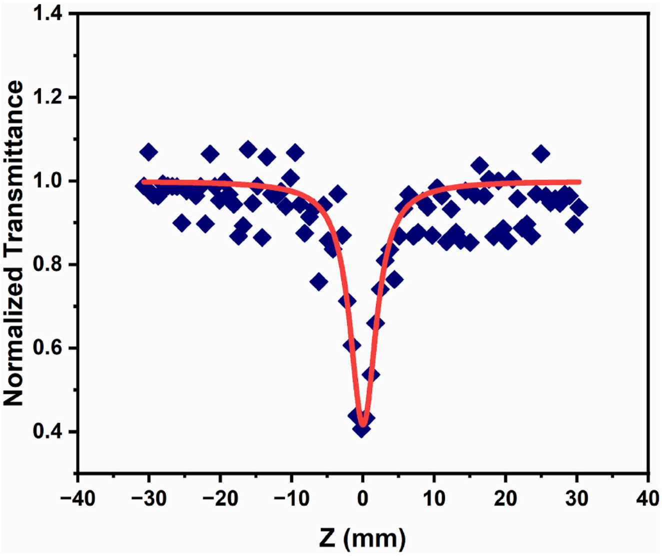

Fig. 15. Open aperture curve of ETPI.

Z_o is the Rayleigh range or diffraction length, I_o is the input intensity of the laser beam, and L_{eff} is the effective length of the sample. The nonlinear absorption in ETPI is attributed to the two-photon absorption process, with theoretical and experimental data findings aligning with each other [58].

The observed reverse saturable absorption in the sample is attributable to a two-photon absorption (2PA) mechanism, as demonstrated by fitting the open-aperture Z-scan data to the established theoretical model for 2PA. Notably, nonlinear reverse saturable absorption may arise from two different pathways within the two-photon absorption process. The first pathway involves a genuine two-photon absorption event, where two photons are absorbed simultaneously, exciting an electron from the ground state to the first excited state. The second pathway involves a sequential 2PA mechanism, in which the first photon elevates the electron to a near-resonant state, followed by a second photon that further excites the electron to a higher excited state. The linear absorption spectral data obtained from the current measurements show significant absorption within the visible spectrum, confirming the presence of a near-resonant state close to the excitation wavelength. Additionally, the dependence of the nonlinear absorption coefficient on the on-axis intensity suggests that nonlinear absorption primarily occurs through the sequential two-photon absorption process.

ETPI demonstrates a broad optical transparency range from 300 to 800 nm, rendering them appropriate for investigations related to optical limiting. The fluence (F(z)) of a filtered Gaussian laser beam at position Z is described by an equation (22) derived from open-aperture Z-scan data.

$$F(z) = 4\sqrt{\ln 2}\left(\frac{E_{in}}{\pi^{\frac{3}{2}}}\right)\omega(z)^2 \tag{22}$$

Where the beam radius can be given by equation (23)

$$\omega(Z) = \omega(0)\left[1 + \left(\frac{z}{z^o}\right)^2\right]^{1/2} \tag{23}$$

ω (0) is the focal spot radius, and λ is the excitation wavelength. The open-aperture curve for an on-axis input intensity of 2.46×10^2 W/m^2 shows that the ETPI crystal exhibits optical limiting behaviour due to reverse saturable absorption [59–61].

Fig. 16 shows the normalised transmittance versus input intensity (W/m^2), highlighting the material's optical limiting properties with an onset optical limiting threshold of 3.41×10^{12} W/m^2. A lower threshold increases the optical limiting effect. Table 5 lists the nonlinear optical absorption coefficient (β), saturation intensity (I_S), and onset optical limiting threshold for the title crystal, indicating that ETPI crystals are suitable for protecting against high-intensity laser exposure [62–64].

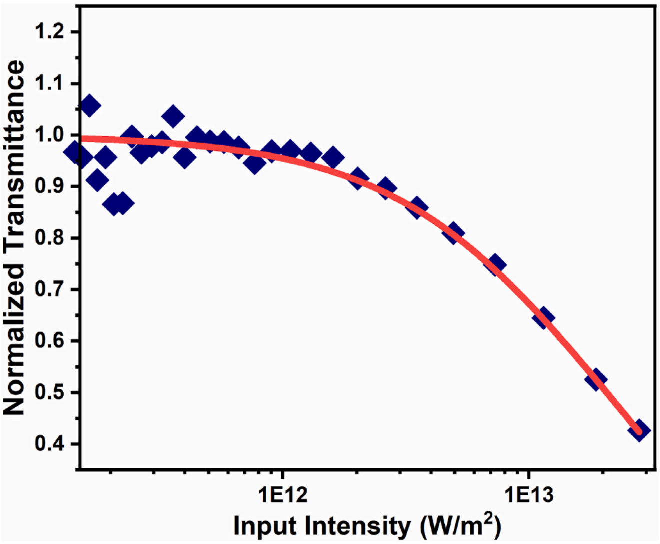

Fig. 16. Normalised transmittance vs Input intensity (W/m^2).

Table 5
Third-order NLO parameters of ETPI.

Sample Name	Saturation Intensity, I_S x 10^{11} W/m^2	Nonlinear Absorption Coefficient, β x 10^{-10} m/W	Onset Optical Limiting Threshold, x 10^{12} W/m^2
ETPI	39	0.84	3.41

4. Conclusion

A high-quality nonlinear optical single crystal of Ethyltriphenylphosphonium iodide hydrate was successfully grown using the solvent evaporation method at ambient temperature, resulting in a finely structured monoclinic crystal system. Comprehensive FT-IR analysis enabled the determination of vibrational assignments and the identification of the functional groups inherent in this novel material. Notably, absorption studies demonstrated that the cutoff wavelength of this crystal is precisely 280 nm, marking its potential for various optical applications. Further investigations revealed minimal Urbach energy, along with evaluations of the optical constants, underscoring the defect-free crystalline nature and superior optical quality of the material. The photoluminescence (PL) spectrum exhibited a distinct peak, indicating the presence of remarkable violet fluorescence, which enhances the material's optical appeal. HR-SEM/EDAX provides insights into the crystal's structural characteristics. The recorded damage pattern in response to laser exposure revealed a significant resistance, indicating a power density threshold of 7.5 GW/cm^2, demonstrating the crystal's robust performance under extreme conditions. In terms of electrical properties, the observed photocurrent was found to be lower than that of the dark current, suggesting a characteristic negative photoconductivity nature, which is intriguing for its potential applications in electronic devices. Thermal assessments indicated that the material exhibits commendable thermal stability, with a melting point recorded at 170 °C. Additionally, a systematic evaluation showed an exponential decline in both the dielectric constant and dielectric loss across a varying temperature spectrum as frequency increased, highlighting the material's efficiency in diverse electrical applications. Theoretical evaluations of electronic polarizability further affirm the superior quality of the crystal. Lastly, an in-depth assessment of the third-order nonlinear optical absorption coefficient and the optical limiting threshold was conducted using advanced Z-scan analysis techniques, paving the way for promising applications in the fields of photonics and optoelectronics.

CRediT authorship contribution statement

M. Mohanraj: Writing – original draft, Methodology, Data curation, Conceptualization. **T.C Sabari Girisun:** Writing – review & editing, Validation, Formal analysis, Data curation. **M. Parthasarathy:** Validation, Supervision, Methodology, Investigation, Data curation.

Ethical approval

All experiments were carried out according to university guidelines. None of the authors used human beings as research subjects.

Consent for publication

In the present study, there were no person's data in any form.

Funding declaration statement

The authors did not receive support from any organisation for the submitted work.

Declaration of competing interest

The authors declare that they have no known competing financial interests or personal relationships that could have appeared to influence the work reported in this paper.

Acknowledgement

The authors would like to express their sincere gratitude to Vels Institute of Science, Technology and Advanced Studies (VISTAS), Pallavaram, Chennai-600117, for facilitating this research. We also acknowledge the invaluable contributions of SAIF and IIT-Madras for their assistance in conducting single-crystal X-ray diffraction, FT-IR, UV–visible, photoluminescence, HR-SEM/EDAX, and DSC analyses. Our heartfelt thanks to the Department of Physics, B. S. Abdur Rahman Institute of Science & Technology, Chennai-600048, for their support in performing LDT and dielectric analyses. Additionally, we extend our appreciation to SSN College of Engineering, Chennai-603110, for their role in the photoconductivity measurements.

Data availability

The data presented in this study are available upon request from the corresponding author.

References

[1] J.L. Freeman, Q. Zhao, Y. Zhang, J. Wang, C.M. Lawson, G.M. Gray, Synthesis, linear and nonlinear optical properties of phosphonato-substituted bithiophenes derived from 2,20-biphenol, Dalt. Trans. 42 (2013) 14281, https://doi.org/10.1039/c3dt51499d.

[2] V. Krishnakumar, J. Jayaprakash, S. Boobas, M. Komathi, Synthesis, growth, optical and anisotropic mechanical behaviour of organic nonlinear optical imidazolium 2-chloro-4-nitrobenzoate single crystals, Eur. Phys. J. Plus. 131 (2016) 375, https://doi.org/10.1140/epjp/i2016-16375-0.

[3] K. Nivetha, S. Kalainathan, M. Yamada, Y. Kondo, F. Hamada, Investigation on the growth, structural, HOMO–LUMO and optical studies of 1-ethyl-2-[2-(4 hydroxy-phenyl)-vinyl]-pyridinium iodide (HSPI)– a new stilbazolium derivative for third-order NLO applications, RSC Adv. 6 (2016) 35977–35990, https://doi.org/10.1039/C6RA02544G.

[4] Ajij Golandaj, Akil Ahmad, Deresh Ramjugernath, Phosphonium salts in asymmetric catalysis: a journey in a decade's extensive research work, Adv. Synth. Catal. 359 (2017) 3676–3706, https://doi.org/10.1002/adsc.201700795.

[5] Cai Zhang, Recent developments in trifluoromethylation or difluoroalkylation by use of difluorinated phosphonium salts, Adv. Synth. Catal. 359 (2017) 372–383, https://doi.org/10.1002/adsc.201601011.

[6] Robert Biczak, Piotr Bałczewski, Barbara Pawłowska, Barbara Bachowska, Piotr Rychter, Comparison of phytotoxicity of selected phosphonium ionic liquid, Ecol Chem Eng S 21 (2014) 281–295, https://doi.org/10.2478/eces-2014-0022.

[7] Richard Betz, Thomas Gerber, Ethyltriphenylphosphonium bromide dihydrate, Acta Cryst. E 67 (2011) o1950, https://doi.org/10.1107/S1600536811026559.

[8] Jiayao Y. Wang, Jiaqi Q. Li, Yumei M. Xiao, Bin Fu, Zhaohai H. Qin, Triphenylphosphonium (TPP)-based antioxidants: a new perspective on antioxidant design, ChemMedChem 15 (2020) 404–410, https://doi.org/10.1002/cmdc.201900695.

[9] M. Parthasarathy, R. Gopalakrishnan, Growth, photoluminescence, thermal and mechanical behaviour of Ethyltriphenylphosphonium bromide dihydrate crystal, Opt. Mater. 35 (2013) 2056–2061, https://doi.org/10.1016/j.optmat.2013.05.007.

[10] Samah E.E. Warrag, Ahmad S. Darwish, Idowu A. Adeyemi, Mohamed K. Hadj-Kali, Maaike C. Kroon, Inas M. AlNashef, Extraction of pyridine from n-alkane mixtures using methyltriphenylphosphonium bromide-based deep eutectic solvents as extractive denitrogenation agents, Fluid Phase Equilib. 517 (2020) 112622, https://doi.org/10.1016/j.fluid.2020.112622.

[11] Boris L. Shivachev, Krassimir Kossev, Louiza T. Dimowa, Georgi Yankov, Todor Petrov, Rositsa P. Nikolova, Nadia Petrova, Synthesis, growth, structural, thermal, optical properties of new metal-organic crystals: methyltriphenylphosphonium iodide thiourea and methyltriphenylphosphonium iodide chloroform hemisolvate, J. Cryst. Growth 376 (2013) 41–46, https://doi.org/10.1016/j.jcrysgro.2013.04.040.

[12] Mohamed Khalid Alomar, Mohammed Abdulhakim Alsaadi, Maan Hayyan, Shatirah Akib, Muhammad Ibrahim, Mohd Ali Hashim, Allyl triphenyl phosphonium bromide based DES-functionalized carbon nanotubes for the removal of mercury from water, Chemosphere 167 (2017) 44–52, https://doi.org/10.1016/j.chemosphere.2016.09.133.

[13] Shahriare Ghammamy, Monir Rahnama Baghy, Wong Wing-Tak, Kheiroallah Mehrani, Saied Maleki, Synthesis, characterization, X-ray structural analysis and study of oxidative properties of propyltriphenylphosphonium bromochromate, Transition Met Chem 32 (2007) 257–261, https://doi.org/10.1007/s11243-006-0162-6.

[14] Pavel Valerievich Andreev, Vladimir Viktorovich Sharutin, Olga Konstantinovna Sharutina, Synthesis and structure of ethyltriphenylphosphonium iodide hydrate, Yuzhno-Ural'skii Gosudarstvennyi Universitet, Vestnik. Seriya Khimiya 10 (2018), https://doi.org/10.14529/chem180105, 43-1.

[15] Wei Xiong, Dongying Hu, Fabrication of phosphonium bamboo cellulose by triphenylphosphine: preparation, characterization, and adsorption of Acid Black 24, Environ. Sci. Pollut. Control Ser. 26 (2019) 1880–1891, https://doi.org/10.1007/s11356-018-3711-6.

[16] G. Witschard, C.E. Griffin, Infrared absorption characteristics of alkyl and aryl substituted phosphonium salts, Spectrochim. Acta 19 (1963) 1905–1910, https://doi.org/10.1016/0371-1951(63)80208-8.

[17] J. Balaji, S. Prabu, P. Srinivasan, T. Srinivasan, D. Velmurugan, Studies on the growth and characterization of a nonlinear optical crystal: 3 Hydroxy Pyridinium Tartrate Mono Hydrate (3HPTMH), Spectrochim. Acta Part A Mol. Biomol. Spectrosc. 144 (2015) 139–147, https://doi.org/10.1016/j.saa.2015.01.091.

[18] B. Babu, J. Chandrasekaran, R. Thirumurugan, V. Jayaramakrishnan, K. Anitha, Experimental and theoretical investigation on 2-amino 5-bromopyridinium L tartrate-A new organic charge-transfer crystal for optoelectronics device applications, J. Mater. Sci. Mater. Electron. 28 (2017) 1124–1135, https://doi.org/10.1007/s10854-016-5637-4.

[19] M. Nagaraja, P. Raghu, H.M. Mahesh, Jayadev Pattar, Structural, optical and Urbach energy properties of ITO/CdS and ITO/ZnO/CdS bi-layer thin films, J. Mater. Sci. Mater. Electron. 2 (2021) 8976–8982, https://doi.org/10.1007/s10854-021-05568-4.

[20] Shadia Jamil Ikhmayies, Riyad N. Ahmad-Bitar, A study of the optical bandgap energy and Urbach tail of spray-deposited cds:in thin films, J. Mater. Res. Technol. 2 (3) (2013) 221–227, https://doi.org/10.1016/j.jmrt.2013.02.012.

[21] P. Karuppasamy, Muthu Senthil Pandian, P. Ramasamy, Sunil Verma, Crystal growth, structural, optical, thermal, mechanical, laser damage threshold and electrical properties of triphenylphosphine oxide 4-nitrophenol (TP4N) single crystals for nonlinear optical applications, Opt. Mater. 79 (2018) 152–171, https://doi.org/10.1016/j.optmat.2018.03.041.

[22] Sekar Anand, Muthurakku Usha Rani, Sivaperuman Kalainathan, Ravi Shanker Babu, Analysis of the growth and physicochemical properties of the newly developed stilbazolium derivative 4-N,N-dimethylamino-4-N-methyl stilbazolium 2-formyl benzene sulfonate (DSFS) single crystal: an effective material for nonlinear optical applications, RSC Adv. 12 (2022) 29022–29033.

[23] J. Beena, A.S. Jebamalar, S. Sindhusha, T. Kamalesh, Ynthesis, optimized geometry, optical, electronic, electrical, stability and Z scan analysis of tetra-aqua-bis (p-toluene Sulphonate)-Calcium (PTC) single crystal, Opt. Mater. 133 (2022) 112938, https://doi.org/10.1016/j.optmat.2022.112938.

[24] N. Mahalakshmi, M. Parthasarathy, Spectral Growth, Optical, Dielectric, Laser damage threshold and second harmonic generation studies of L-Threonine single crystals for potential nonlinear optical applications, Eur. Chem. Bull. 12 (2023) 14011–14026, https://doi.org/10.48047/ecb/2023.12.si4.1271.

[25] Helen Merina Albert, Pankaj Dnyanoba Ghodke, Nellore Manoj Kumar, D. Neelima Patnaik, Rajani Indrakanti, B. Uma, M.P. Mallesh, C. Alosious Gonsago, Exploring the spectroscopic, optical, dielectric, and hardness properties of L-histidine methylester dihydrochloride (LHMEDH), a nonlinear optical compound for optoelectronic uses, Appl. Phys. A 130 (2024) 941, https://doi.org/10.1007/s00339-024-08132-z.

[26] R.P. Jebin, T. Suthan, T.R. Anitha, N.P. Rajesh, G. Vinitha, Growth and characterization of organic material 3,4-dimethoxybenzaldehyde-2,4-dinitroaniline single crystal, J. Mater. Sci. Mater. Electron. 32 (2021) 3232–3246.

[27] M. Senthil Pandian, P. Karuppasamy, T. Kamalesh, P. Ramasamy, Sunil Verma, Growth of 2-amino 4,6-dimethyl pyrimidine 4-nitrophenol (AMP4N) single crystals for technological applications, AIP Conf. Proc. 2115 (2019) 030396, https://doi.org/10.1063/1.5113235.

[28] P. Anandan, S. Vetrivel, R. Jayavel, C. Vedhi, G. Ravi, G. Bhagavannarayana, Crystal growth, structural and photoluminescence studies of L-tyrosine hydrobromide semi organic single crystal, J. Phys. Chem. Solid. 73 (2012) 1296–1301, https://doi.org/10.1016/j.jpcs.2012.06.015.

[29] J.H. Joshi, S. Kalainathan, D.K. Kanchan, Ketan Chaudhari, M.J. Joshi, K.D. Parikh, Crystal growth, structural, optical, photoluminescence, electrical and third-order nonlinear optical studies of pure and methylene blue dye-doped ammonium dihydrogen phosphate crystals, J. Mater. Sci. Mater. Electron. 34 (2023) 21, https://doi.org/10.1007/s10854-022-09447-4.

[30] P. Shenbagarajan, P. Jayaprakash, S. Krishnan, S. Selvaraj, T.C. Sabari Girisun, An extensive investigation of the structural, spectral, optical, electrical, and nonlinear optical properties of a single crystal of Di-aqua nitrato bis L-valine lead (II) nitrate, Opt. Mater. 144 (2023) 114337, https://doi.org/10.1016/j.optmat.2023.114337.

[31] G. Peramaiyan, P. Pandi, N. Vijayan, G. Bhagavannarayana, R. Mohan Kumar, Crystal growth, structural, thermal, optical and laser damage threshold studies of 8-hydroxyquinolinium hydrogen maleate single crystals, J. Cryst. Growth 375 (2013) 6–9, https://doi.org/10.1016/j.jcrysgro.2013.04.011.

[32] S. Surya, B. Gunasekaran, Material synthesis, crystal growth, physico-chemical properties and second-order NLO activities of a novel L-histidinium phthalate potassium iodide (LHPPI) single crystal for NLO application, J. Mater. Sci. Mater. Electron. 33 (2022) 26383–26396, https://doi.org/10.1007/s10854-022-09319-x.

[33] L.R. Latha, P. Selvarajan, J. Uma Maheswari, Synthesis and Characterization of L-Proline Potassium Iodide Crystal, vol. 13, 2022, p. 9, https://doi.org/10.55218/JASR.202213913.

[34] K. Rajesh, A. Mani, V. Thayanithi, P. Praveen Kumar, Optical, thermal, and mechanical properties of L-Serine phosphate, a semiorganic enhanced NLO single crystal, Int. J. Optics 2016 (2016) 5, https://doi.org/10.1155/2016/9070714.

[35] C. Senthil Kumar, P. Rajesh, P. Ramasamy, Crystal growth, spectral, optical, laser damage, photoconductivity and dielectric properties of semi organic l-cystine hydrochloride single crystal, Spectrochim. Acta Mol. Biomol. Spectrosc. 151 (2015) 432–437, https://doi.org/10.1016/j.saa.2015.06.113.

[36] K. Rajesh, A. Arun, A. Mani, P. Praveen Kumar, Crystal growth, perfection, linear and nonlinear optical, photoconductivity, dielectric, thermal and laser damage threshold properties of 4-methylimidazolium picrate: an interesting organic crystal for photonic and optoelectronic devices, Mater. Res. Express 3 (2016) 106203, https://doi.org/10.1088/2053-1591/3/10/106203.

[37] J. Arumugam, M. Selvapandiyan, C. Senthilkumar, M. Srinivasan, P. Ramasamy, Crystal growth, optical, thermal, laser damage threshold, photoconductivity and third-order nonlinear optical studies of KCl doped sulphamic acid single crystals, 6084–6096, https://doi.org/10.1007/s10854-020-03161-9, 2020.

[38] Suresh Sagadevan, Priya Murugasen, Microhardness Growth, Electrical and dielectric studies on L-Alanine hydrogen chloride NLO single crystal, Int. J. Mater. Sci. Eng. 3 (2015) 159–166, https://doi.org/10.17706/ijmse.2015.3.2.159-166.

[39] Koteeswari Pandurangan, Sagadevan Suresh, Synthesis, growth, and characterization of bisglycine hydrobromide single crystal, J. Mater. Sci. 2014 (2014) 7, https://doi.org/10.1155/2014/362678.

[40] S. Suresh, The growth and the optical, mechanical, dielectric and photoconductivity properties of a new nonlinear optical Crystal—L-Phenylalanine-4-nitrophenol NLO single crystal, J. Cryst. Process Technol. 3 (2013) 3, https://doi.org/10.4236/jcpt.2013.33014.

[41] Apurva Gupta, M.K. Raseel Rahman, Romu Jauhar, V. Sivasubramani, N. Vijayan, G. Vinitha, Lekha Nair, Growth of L-asparagine monohydrate and its structural, optical, mechanical, thermal and electrical studies for nonlinear optical applications, Mater. Res. Express 6 (2020) 125119, https://doi.org/10.1088/2053-1591/ab7a5d.

[42] Sudha Yadav, Mukesh Jewariya, Manju Kumari, Debabrata Nayak, N. Vijayan, T. Mondal, Crystal growth and optical, nonlinear optical, thermal and terahertz time domain spectra of l-Histidine single crystal: a potential terahertz material, ACS Appl. Opt. Mater. 11 (2023) 1791–1800, https://doi.org/10.1021/acsaom.3c00243.

[43] S. Thangavel, V. Kathiravan, R. Ashok Kumar, S. Eniya, G. Satheesh Kumar, P. Selvarajan, M. Kumaresavanji, Crystal growth of l-Alanine oxalic acid crystal and its spectral, NLO, mechanical, thermal, and impedance properties, J. Electron. Mater. 51 (2022) 3068–3077, https://doi.org/10.1007/s11664-022-09546-2.

[44] P. Revathi, T. Balakrishnan, J. Thirupathy, An investigation on optical, dielectric and thermal analysis of semiorganic bisglycine cobalt chloride dihydrate single crystal for electronic and opto-electronic devices, Opt. Quant. Electron. 56 (2024) 1804, https://doi.org/10.1007/s11082-024-07713-9.

[45] B.R. Thejashwini, Vijay Khopkar, R. Madhusudhana, B. Sahoo, Crystal growth and effect of defects on the dielectric properties of ammonium dihydrogen phosphate (ADP) single crystals, J. Mater. Sci. Mater. Electron. 31 (2020) 10548–10552, https://doi.org/10.1007/s10854-020-03603-4.

[46] Si-Min, LiuYing-Jie Cao, Lei He, Ping-Ping Shi, Qiong Ye, Phosphonium-based one-dimensional perovskite with switchable dielectric behaviors and phase transitions, Inorg. Chem. 59 (2020) 18396–18401, https://doi.org/10.1021/acs.inorgchem.0c03008.

[47] B. Uma, K. Sakthi Murugesan, S. Krishnan, R. Jayavel, B. Milton Boaz, Growth, optical, thermal and dielectric studies of a highly polarisable semi organic NLO crystal: Bis d-phenyl glycinium sulphate monohydrate, Mater. Chem. Phys. 142 (2013) 659–666, https://doi.org/10.1016/j.matchemphys.2013.08.018.

[48] T. Kamalesh, P. Karuppasamy, Muthu Senthil Pandian, P. Ramasamy, Sunil Verma, Synthesis, crystal growth, and physicochemical characterization of 4-aminopyridinium 4-nitrophenolate 4-nitrophenol (4AP4NP) single crystals for NLO applications, J. Mater. Sci. Mater. Electron. 32 (2021) 6141–6157, https://doi.org/10.1007/s10854-021-05332-8.

[49] J.D. Jackson, Classical Electrodynamics, Wiley Eastern, 1978, p. 321.

[50] D.R. Penn, Wave-number-dependent dielectric function of semiconductors, Phys. Rev. 128 (1962) 2093–2097, https://doi.org/10.1103/PhysRev.128.2093.

[51] N.M. Ravindra, R.P. Bharadwaj, K.S. Kumar, V.K. Srivastava, Model based studies of some optical and electronic properties of narrow and wide gap materials, J. Infrared Phys. 21 (1981) 369, https://doi.org/10.1016/0020-0891(81)90045-2.

[52] N.M. Ravindra, V.K. Srivastava, Electronic polarizability as a function of the penn gap in semiconductors, J. Infrared Phys. 20 (1980) 67–69, https://doi.org/10.1016/0020-0891(80)90009-3.

[53] G. Marudhu, S. Krishnan, T. Thilak, P. Samuel, G. Vinitha, G. Pasupathi, Optical, thermal and mechanical studies on nonlinear optical material diglycine barium chloride monohydrate (DGBCM) single crystal, J. Nonlinear Opt. Phys. Mater. 22 (2013) 1350043, https://doi.org/10.1142/S0218863513500434.

[54] M.J. Renne, B.R.A. Nijboer, Microscopic derivation of macroscopic Van der Waals forces, Chem. Phys. Lett. 1 (1967) 317–320, https://doi.org/10.1016/0009-2614(67)80004-6.

[55] B.R.A. Nijboer, M.J. Renne, Microscopic derivation of macroscopic van der waals forces. II, Chem. Phys. Lett. 2 (1968) 35–38, https://doi.org/10.1016/0009-2614(68)80141-1.

[56] S. Vediyappan, R. Arumugam, P. Karuppasamy, R. Kasthuri, M. Senthil Pandian, P. Ramasamy, Crystal growth and characterization of semi-organic 2-amino-5-nitropyridinium bromide (2A5NPBr) single crystals for third-order nonlinear optical (NLO) applications, Appl. Phys. A 123 (2017) 780, https://doi.org/10.1007/s00339-017-1394-3.

[57] S. Hemavathy, G. SanthanaKrishnan, T.C. Sabari Girisun, M. Parthasarathy, Investigation on growth, structural, spectral, DFT, MEP computational studies of novel methyl triphenylphosphonium bromide hydrate single crystal for third-order nonlinear optical limiting applications, J. Mol. Struct. 15 (2025) 140968, https://doi.org/10.1016/j.molstruc.2024.140968.

[58] T. Thilak, M. Basheer Ahamed, G. Vinitha, Third order nonlinear optical properties of potassium dichromate single crystals by Z-scan technique, Optik 124 (2013) 4716–4720, https://doi.org/10.1016/j.ijleo.2013.01.111.

[59] N. Mahalakshmi, S.R. Meeraa, G. Vinitha, M. Parthasarathy, Synthesis, growth, photoluminescence, thermal, and third-order nonlinear optical properties of glycine methyl ester hydrochloride single crystal for opto-electronic applications, Braz. J. Phys. 54 (2024) 49, https://doi.org/10.1007/s13538-024-01420-2.

[60] R. Ragu, M. Akilan, J.P. Angelena, P.S. Latha Mageshwari, S. Jerome Das, Growth, optical, mechanical, thermo-physical, laser damage threshold (LDT) and Z-scan studies on dilithium succinate single crystal for optical limiting applications, J. Mater. Sci. Mater. Electron. 30 (2019) 6287–6299, https://doi.org/10.1007/s10854-019-00933-w.

[61] S.R. Meeraa, M. Parthasarathy, Synthesis and characterization of single crystals of creatininium hydrochloride for third-order NLO applications, Cryst. Res. Technol. 59 (2024) 2300133, https://doi.org/10.1002/crat.202300133.

[62] Anıl Dogan, Ahmet Karatay, Mehmet Isik, Elif Akhuseyin Yıldız, Nizami Mamed Gasanly, Ayhan Elmali, Revealing the effects of defect states on the nonlinear absorption properties of the TlInsse and $Tl_2In_2S_3Se$ crystals in near-infrared optical limiting applications, Cryst. Growth Des. 24 (2024) 6981–6990, https://doi.org/10.1021/acs.cgd.4c00606.

[63] Yasemin Pepe, Elif Akhuseyin Yildiz, Mehmet Isik, Ahmet Karatay, Nizami Gasanly, Ayhan Elmali, Tunable nonlinear absorption and optical limiting behavior of $NaBi(Mo_xW_{1-x}O_4)_2$ single crystals with ratio of molybdenum/tungsten, Phys. Scr. 98 (2023) 075922, https://doi.org/10.1088/1402-4896/acdb03.

[64] Anıl Doğan, Ahmet Karatay, Ayhan Elmali, Mehmet Isik, Elif Akhuseyin Yildiz, Nizami Gasanly, Ayhan Elmali, Revealing photoluminescence and nonlinear optical absorption characteristics of $PbMo_{0.75}W_{0.25}O_4$ single crystal for optical limiting applications, Phys. Scr. 99 (2024) 055546, https://doi.org/10.1088/1402-4896/ad3aee.